

# Modeling Non-Force-Free and Deformed Flux Ropes in Titan's Ionosphere

C. J. Martin<sup>1</sup>, C. S. Arridge<sup>1</sup>, S. V. Badman<sup>1</sup>, D. D. Billett<sup>1,3</sup>, C. J. Barratt<sup>2</sup>

<sup>1</sup>Physics Department, Lancaster University, Bailrigg, Lancaster, LA1 4YB, United Kingdom.

<sup>2</sup>School of Mathematics, Statistics and Physics 4th Floor, Herschel Building Newcastle University, NE1 7RU, United Kingdom

<sup>3</sup>Institute of Space and Atmospheric Studies, University of Saskatchewan, Saskatoon, Canada

## Key Points:

- Various models are fitted to 85 flux ropes that were detected in Titan's ionosphere
- A non-force-free model is a more suitable fit statistically compared to a force-free model, implying flux ropes are dynamic at Titan
- Various deformations that can act on a flux rope are explored, and in some cases an elliptical cross-section is more appropriate than circular

---

Corresponding author: C. J. Martin, [carleymartin@hotmail.com](mailto:carleymartin@hotmail.com)

**Abstract**

Previous work at Titan presented a set of 85 flux ropes detected during Cassini flybys of Titan from 2005-2017. In that study a force-free model was used to determine the radii and axial magnetic field of the flux ropes. In this work we apply non-force free models. The non-force-free model shows an improvement in the number of flux ropes that can be fitted with a model, along with improved uncertainties and  $\chi^2$  values. A number of asymmetries and features in the magnetometer data cannot be reproduced by either model, therefore we deform the force-free model to show that small deformations can replicate these features. One such deformation is to use an elliptical cross-section which replicates a plateau in magnetic field strength along with asymmetries on either side of the centre of the flux ropes. Additionally, we explore the properties of bending a flux rope, where we find that minimum variance analysis becomes increasingly degenerate with bending, along with a slight bend causing the switching of the axial field direction from intermediate to maximum variance direction. We conclude that the flux ropes at Titan show aspects of developing flux ropes, compared to other planetary bodies which exhibit more agreement to the force-free assumptions of mature flux ropes.

**1 Introduction**

Flux ropes are a magnetic phenomena found in most plasma and magnetic field regimes across the solar system and can be found in the solar wind (Burlaga et al., 1982), on the solar surface (e.g., Mouschovias & Poland, 1978), in the magnetospheres of Mercury, Earth and Saturn (e.g., C. T. Russell & Elphic, 1979; Hughes & Sibeck, 1987; Slavin et al., 2010; Jasinski et al., 2016) and in the ionospheres of Venus and Mars (e.g., C. Russell & Elphic, 1979; Vignes et al., 2004). Flux ropes are bundles of magnetic flux, which is twisted around a central axis. They are a result of an interactive and dynamic plasma and magnetic environment. Taking a cross-section, the flux rope appears to have a purely tangential field at the edges which reduces in the centre where an axial field is dominant. Flux ropes could be a diagnostic tool to uncover the dynamical interaction with the ionosphere and surrounding magnetic field. On the solar surface flux ropes are thought to be a precursor to coronal mass ejections Chen and Shibata (2000).

Titan is Saturn's largest moon and is home to a large, extended atmosphere that is over 1000 km thick (Yelle et al., 2006) due to the lower gravity and higher density than at Earth. As such, Titan's ionospheric electron density peak, in comparison, sits at a much higher altitude of 1100 - 1200 km (Keller et al., 1992; Ågren et al., 2009). The ionosphere is mainly formed though magnetospheric electron impacts and solar radiation (e.g., Cravens et al., 2005; Ågren et al., 2007) along with other sources. Titan has no measured internal magnetic field and as such the interaction between the ionosphere and the exterior magnetic field forms an induced magnetosphere, similar to that at Venus, in the form of draped magnetic field lines which are 'captured' by the ionospheric plasma (Ness et al., 1982).

Flux ropes in Titan's ionosphere were first reported by Wei et al. (2010), where the authors find instances of increased magnetic field magnitude in Cassini magnetometer data. These magnetic field signatures were compared to a force-free flux rope model (e.g., Burlaga, 1988) to conclude that they were indeed flux ropes. The authors also compare these flux ropes to similar instances of flux ropes in Venus' ionosphere which are considered more mature than the flux ropes at Titan. Additionally, Wei et al. (2011) recorded an unusually large peak in magnetic field magnitude during the T42 flyby which exceeded all previous measurements at Titan. This structure was shown to be a large flux rope and the authors discuss a possible source in the interaction with solar wind plasma when Saturn's magnetopause was pushed back inside Titan's orbit in the recent past. Additional possible formation mechanisms are also discussed in Martin et al. (Accepted).

64 Further to this, Martin et al. (Accepted) found 85 instances of flux ropes in the iono-  
 65 sphere of Titan and showed statistically that they are larger on average than those at  
 66 Venus and are found in locations of higher dynamic magnetic environments. The authors  
 67 also fitted a force-free flux rope model to the examples found, however they found that  
 68 just over half of the flux ropes fitted adequately to the force-free assumptions and as such  
 69 further study is needed to determine a more accurate model to represent the flux ropes  
 70 in Titan’s ionosphere. This study presents the force-free model results along side a non-  
 71 force-free approach to compare the two models. Additionally, deformations to the flux  
 72 ropes are examined, such as elliptical cross sections and bent flux ropes, to examine if  
 73 the flux ropes themselves are dynamic structures that require more than a simple cylin-  
 74 drically symmetric, stationary model to accurately portray.

75 Elphic and Russell (1983a, 1983b) described a flux rope as a discrete individual ex-  
 76 cursion of magnetic field, where a peak in magnetic field magnitude is larger than the  
 77 surrounding magnetic field. Using this description, flux ropes are detected using the Cassini  
 78 magnetometer (Dougherty et al., 2004) data set during all of Cassini’s Titan flybys. An  
 79 example of two altitude plots with single flux ropes on flybys T30 and T84 are shown  
 80 in figure 1 of the companion paper Martin et al. (Accepted).

81 Historically, most studies (e.g., C. Russell & Elphic, 1979; Vignes et al., 2004; Wei  
 82 et al., 2010; Jasinski et al., 2016; Martin et al., Accepted) rely on minimum variance anal-  
 83 ysis (MVA) (Sonnerup & Cahill Jr, 1967) to rotate the magnetic field into a flux rope  
 84 aligned cylindrical coordinate system. Some studies have circumvented MVA by explic-  
 85 itly including the orientation angles as free parameters in the mode (e.g., Hidalgo et al.,  
 86 2002) or using geometrical assumptions (e.g., Li et al., 2016). However, MVA remains  
 87 the most convenient method for automatic reorientation of the coordinate systems.

88 Martin et al. (Accepted) discussed that in a pure mathematical sense, the axial field  
 89 direction is found as the intermediate variance direction, and the tangential field direc-  
 90 tion is found mainly in the maximum field direction, where the minimum variance di-  
 91 rection is a constant zero. At Titan, however, the axial field is commonly found as the  
 92 maximum variance direction and the tangential field is found as the intermediate direc-  
 93 tion. In this study we will present a force-free model using orientation angles rather than  
 94 the use of MVA, along with a bent flux rope model which assesses the validity of MVA  
 95 as we diverge from a pure mathematical explanation of how MVA operates in non-ideal  
 96 situations. Additionally, we develop a force-free elliptical flux rope model to discuss the  
 97 validity of the circular cross-section assumption of other models, along with a compar-  
 98 ison of purely force-free and non-force-free models.

## 99 2 Model Comparison

100 The force-free model assumes that  $\mathbf{j} \times \mathbf{B}$  force density is equal to zero and as such  
 101 any currents present are field aligned or zero valued. This also means that then mag-  
 102 netic tension force in the flux rope  $\left(\frac{B^2}{2\mu_0 R_c}\right)$  is balanced with the magnetic pressure force  
 103  $\left(\frac{B^2}{2\mu_0}\right)$ , where  $B$  is magnetic field magnitude,  $\mu_0$  is the permeability of free space and  
 104  $R_c$  is the radius of curvature. (Osherovich et al., 1995) emphasises that the force-free  
 105 assumptions shows that the flux rope is in the lowest energy state, and hence is in equi-  
 106 librium or *mature*. This idea is further discussed by (Wei et al., 2010), inferring that a  
 107 developing flux rope would not appear as force-free.

108 As described earlier, MVA can be used to rotate the magnetic field data into flux  
 109 rope coordinates, where the variance directions at Titan are different to those found at  
 110 other planetary bodies (i.e., Mercury Slavin et al., 2010). There are numerous caveats  
 111 in using MVA and as such the success of fitting a force-free model based on the use of  
 112 MVA is dependent on the degeneracy of the variance directions (Sonnerup & Cahill Jr,

113 1967) and the path of the spacecraft through the structure (Xiao et al., 2004). As such  
 114 if the variance directions are degenerate then MVA is unable to rotate the magnetic field  
 115 data into the flux rope coordinate system. However, one can include orientation angles  
 116 in the fitting process to possibly improve the success rate (e.g., Hidalgo et al., 2002).

117 In cylindrical coordinates, the force-free model reads:

$$118 \quad B_A = B_0 J_0(\alpha R) + b_0, \quad (1)$$

$$119 \quad B_T = H B_0 J_1(\alpha R), \quad (2)$$

$$120 \quad B_R = 0, \quad (3)$$

120 where,  $B_0$  is the central magnetic field,  $J_0$  and  $J_1$  are the zeroth and first order Bessel  
 121 functions,  $\alpha$  is the first root of the zeroth order Bessel function, 2.4048.  $R$  is the radial  
 122 distance to the centre of the flux rope,  $b_0$  is a magnetic offset and  $H$  is the handedness  
 123 of the flux rope or which way the flux rope twists around the center and takes the value  
 124 1 for right-handed ropes, and -1 for left-handed ropes.

125 This is then updated to include the orientation angles,  $\gamma$ ,  $\eta$  and  $\nu$ , which describe  
 126 the orientation of the centre of the flux rope axis in TIIS (Titan Ionospheric Interaction  
 127 System) coordinates. These angles represent the three Euler angles required to rotate  
 128 a coordinate system. In the model,  $R$  is an input vector describing the radial distance  
 129 from the centre of the flux rope, as we do not know  $R$ , we use a proxy  $u$  which ranges  
 130 from -1 to 1 along Cassini's trajectory to estimate  $\alpha R$  in the following equation.

$$131 \quad \alpha R = 2.40 \left( \sqrt{\left(\frac{Y_0}{R_0}\right)^2 + u^2 \left(1 - \left(\frac{Y_0}{R_0}\right)^2\right)} \right), \quad (4)$$

131 where  $Y_0$  is the distance fo closest approach,  $R_0$  is the radius and  $\frac{Y_0}{R_0}$  is the impact  
 132 factor which equals 1 at the flux rope edge and 0 at the center (Lepping et al., 2017). As  
 133  $Y_0$  and  $R_0$  are both dependent on  $R_0$ , this means that we must fit the impact factor rather  
 134 than the two separately and the radius must be found geometrically using the follow-  
 135 ing equation, the spacecraft velocity  $V$  (assuming a stationary flux rope), the angle be-  
 136 tween the flux rope axis and the trajectory subtracted from  $90^\circ$  ( $\phi$ ), and time in seconds  
 137 ( $t$ ).

$$138 \quad R_0 = \frac{V t \cos(\phi)}{2 \sin \left( \arccos \left( \frac{Y_0}{R_0} \right) \right)}, \quad (5)$$

138 Alternatively to the previous force-free study (Martin et al., Accepted) which uses a non-  
 139 linear least-squares fitting technique, this model is fitted using the Bayesian regression  
 140 concept where each parameter is given an initial probability distribution, which is then  
 141 sampled and a  $\chi^2$  value for one sample of each distribution is found. If the  $\chi^2$  is below  
 142 the acceptable threshold then the sample is retained, if it is above it is discarded. This  
 143 is repeated until 10,000 samples give a *posterior* distribution of acceptable  $\chi^2$  for each  
 144 parameter. This process allows easy control over an initial test space for each param-  
 145 eter, probes the entire  $\chi^2$  and avoids the caveats of using a least-squares fitting algorithm.  
 146 The modal value of each parameter's posterior distribution is taken as the fitted value  
 147 and a credible interval is found where 30% of all of the posterior distribution is inside  
 148 the interval and is considered the uncertainty in the parameter (this value is compar-  
 149 able to a standard deviation estimate of uncertainty).

150 Force-free model results are shown statistically in figure 2, along with two exam-  
 151 ples of fitted flux ropes in figures 3 & 4 in blue.

152 The non-force-free model is based on the Hidalgo et al. (2002) model, used to de-  
 153 termine size and currents inside a magnetic cloud in the solar wind. This model used ge-  
 154 ometry of the spacecraft trajectory and predictable direction of propagation of magnetic

155 clouds to fit angles of rotation, and as such does not require MVA. Nieves-Chinchilla et  
 156 al. (2016) generalised the model into the flux rope coordinate system by fitting the cur-  
 157 rents as a polynomial expansion. Thus, the currents are fitted and as such may not be  
 158 restricted to only the parallel direction or a zero value.

$$B_R = 0, \tag{6}$$

$$B_A = B_A^0 + \mu_0 \int_0^r j_T(r) dr = B_A^0 + \mu_0 \sum_{n=1}^{\infty} \alpha_n \frac{1}{n+1} r^{n+1}, \tag{7}$$

$$B_T = -\frac{\mu_0}{r} \int_0^r r j_A(r) dr = -\mu_0 \sum_{m=0}^{\infty} \beta_m \frac{r^{m+1}}{m+2}, \tag{8}$$

161 where  $B_A^0$  is a boundary condition of the flux rope where in this study an infinitely tan-  
 162 gential field is found at the flux rope radius,  $B_A^0 = \mu_0 \sum_{n=1}^{\infty} \alpha_n \frac{1}{n+1} R^{n+1}$ , where  $R$  is  
 163 the flux rope radius.  $r$  is radial distance,  $j_T(r)$  and  $j_A(r)$  are the tangential and axial  
 164 current densities which are modelled as polynomial expansions  $\mathbf{j} = \sum_{m=0}^{\infty} \beta_m r^m \mathbf{e}_A -$   
 165  $\sum_{n=1}^{\infty} \alpha_n r^n \mathbf{e}_T$  with polynomial coefficients  $\alpha_n$  and  $\beta_m$ .  $\mu_0$  is the permeability of free space.  
 166 Handedness of the rope is included in the sign on  $j_A$  where +1 is right and -1 is left-handed.

167 The boundary condition can be changed to give a smoother transition into a sur-  
 168 rounding medium, or to give the magnetic field at the flux rope radius a larger axial  
 169 direction, however we retain the assumption of tangential field at the radius and a gen-  
 170 eral discussion of changes in this parameter are discussed further in Nieves-Chinchilla  
 171 et al. (2016). The maximum central field strength can be calculated using parameters  
 172 fitted for each flux rope at radius  $r = 0$ . The fitting method used is the Bayesian re-  
 173 gression method described above, including the three Euler angles to rotate into a flux  
 174 rope coordinate system. Uncertainties in each parameter are estimated through the use  
 175 of a credible interval of 30%.

176 The order of the polynomials were determined by trial-and-error. Expansions above  
 177 3rd for the axial current, and 4th order for the tangential current were found to produce  
 178 much smaller incremental steps in lowering  $\chi^2$ , which were outweighed by the added com-  
 179 putation time. As such, 3rd and 4th order polynomials were found to be the most eco-  
 180 nomical in time when automating the process.

181 Non-force-free model results are shown statistically in figure 2, along with two ex-  
 182 amples of fitted flux ropes in figures 3 & 4 in red. Position, central magnetic field and  
 183 size derived from the non-force-free model is displayed in figure 1, where little spatial re-  
 184 lationship is displayed over the two fitted variables. Figures 3 & 4 show the fitting of the  
 185 force-free model (blue) and the non-force-free model (red) to the Cassini magnetome-  
 186 ter data (black). The figures show the axial and tangential magnetic field and current  
 187 density, along with a computed  $\mathbf{j} \times \mathbf{B}$  force density. The force-free model shows near zero  
 188 values current densities and  $\mathbf{j} \times \mathbf{B}$  force density, where the uncertainty areas have been  
 189 removed as they cover the whole window, showing that these parameters are valued at  
 190 zero within uncertainties.

191 Both models are symmetrical around the peak in the axial field direction, however  
 192 the non-force-free model appears to fit within uncertainties to the magnetometer data  
 193 to a better degree. This is reflected in the  $\chi^2$  value where the force-free gives values of  
 194 6.9364 nT for Figure 3 and 3.5182 nT for Figure 4. Both are acceptable values of fit ( $\chi^2$   
 195  $< 5$ ), however, the non-force-free model gives values of 0.39752 and 0.47076 nT, which  
 196 shows that the model is over-fitting (uncertainty in the model is larger than the aver-  
 197 age difference between the model and the data).

198 The non-force-free model shows much larger (and non-zero) values within uncer-  
 199 tainties in current density values along with  $\mathbf{j} \times \mathbf{B}$ . The current densities can be con-

200 considered near field aligned in these examples as axial current density shows a peak in mag-  
 201 nitude near the magnetic field peak in figure 3. However, the magnitude is much smaller  
 202 than the tangential current density. In figure 4 the axial current density declines across  
 203 the whole flux rope, however the tangential current density shows a similar relation with  
 204 radius.

205 Both figures show a quasi-sinusoidal relationship with radius for the  $\mathbf{j} \times \mathbf{B}$  force  
 206 density, where the edges of the flux rope show the highest magnitude in figure 4 but at  
 207 half the radius in figure 3, where the force density is expected to be in the radially out-  
 208 ward direction.

209 Figure 2 shows the statistical comparison between the force-free (blue) and non-  
 210 force-free (red) models for all flux ropes that are fitted (49 for force-free, 84 for non-force-  
 211 free). The figure shows that on average the models give similar results of 1-15 nT for ax-  
 212 ial magnetic field, 50-500 km for radius both with larger ranges. However, Figures (3 & 4)  
 213 show two examples where the difference in values is large. These values are summarised  
 214 in table 1 and suggest that the closest approach of Cassini to the centre of the flux rope  
 appears to strongly affect the agreement of the models.

Method	Figure 3: Radius [km]	12/05/2007 Magnetic Field [nT]	CA	Figure 4: Radius [km]	16/04/2005 Magnetic Field [nT]	CA
FF	$53 \pm 7$	$6.6 \pm 2.3$	0.7	$115 \pm 11$	$13.5 \pm 2.2$	0.3
NFF	$132 \pm 11$	$9.6 \pm 3.5$	0.7	$119 \pm 11$	$14.1 \pm 3.4$	0.3

**Table 1.** Comparison of parameters corresponding to figures 3 and 4.

215

### 216 3 Deviations from Cylindrical Symmetry

217 In the confines of this study, we define a bent flux rope as a flux rope that does not  
 218 have a straight axis. In both the previously discussed models and in Martin et al. (Ac-  
 219 cepted) the assumption is that the axis of the flux rope does not move or diverge from  
 220 a straight configuration during Cassini’s fly-through. However, we often find that an asym-  
 221 metry in the magnetic field data is present where both axial and tangential field is skewed  
 222 where one side has a steeper gradient than the other towards the peak - where the peak  
 223 is assumed to be the centre of the flux rope. Figure 5 shows a diagrammatic sketch of  
 224 a bent flux rope, with a cut out to show the increasingly axial field, along with the ex-  
 225 pected magnetic field signatures for the shown fly-through.

226 To model a bent flux rope, we utilise the force-free model described in a previous  
 227 section which is then deformed using the Tsyganenko (1998) general deformation method.  
 228 The force-free model to obtain an undeformed magnetic field which is then deformed spa-  
 229 tially by a parabola in the x-direction where the original z-axis is the undeformed flux  
 230 rope axis,

$$z = ax^2, \tag{9}$$

231 and  $a$  is the leading co-efficient of the polynomial, describing the extent of the bending.  
 232 The normal to the z-axis is then calculated by finding the derivatives of the above equa-  
 233 tion:

$$\frac{dz}{dx} = 2a(x - c), \tag{10}$$

234

$$\frac{dz}{dy} = 2a(y - c), \tag{11}$$

235 where  $c$  is the offset from the  $y$ -axis that the flux rope has moved at the height of the  
 236 parabola. To deform using the general deformation method, a normalised normal vec-  
 237 tor  $(n_x, n_y, n_z)$ , Y-vector  $(Y_x, Y_y, Y_z)$  and X-vector  $(X_x, X_y, X_z)$  are found from the above  
 238 equations, the undeformed  $y$ -axis and the cross product of the normal and Y-vector, re-  
 239 spectively. Hence, we can now build the new deformed coordinate system as:

$$x^* = xX_x + yX_y + zX_z \quad (12)$$

$$y^* = xY_x + yY_y + zY_z \quad (13)$$

$$z^* = xn_x + yn_y + zn_z \quad (14)$$

242 We can now form the new magnetic field in the undeformed coordinate system denoted  
 243 with an asterisk.

$$B_z^* = B_0 J_0(\alpha r^*) + b_0, \quad (15)$$

$$B_x^* = -HB_0 J_1(\alpha r^*) \sin(\phi), \quad (16)$$

$$B_y^* = HB_0 J_1(\alpha r^*) \cos(\phi), \quad (17)$$

246 where  $r^* = \sqrt{x^{*2} + y^{*2}}$ , and  $\phi$  is calculated as the angle of the simulated spacecraft  
 247 from the  $x$ -axis for each position to convert the force-free cylindrical model to a Carte-  
 248 sian coordinate system. The transformation matrix is then formed to give the new mag-  
 249 netic field in the deformed system  $\mathbf{B}'$  where the full expansion of  $\mathbf{T}$  is found in general  
 250 terms in Tsyganenko (1998).

$$\mathbf{B}' = \mathbf{T}\mathbf{B}^* \quad (18)$$

251 An example of a modelled deformed (red) and undeformed (grey) force-free flux rope is  
 252 shown in figure 6, where it is shown that the asymmetry in the  $z$ -component of magnetic  
 253 field is reproduced in Cartesian coordinates. However, the  $x$ - and  $y$ -components do not  
 254 show any asymmetry and both cross the expected centre of the flux rope at 0 seconds.

255 Discussed earlier is the dependence on either MVA or angles in fitting any model  
 256 to flux ropes. However, analysis of flux ropes at different planetary bodies find the vari-  
 257 ance directions as different components of the magnetic field. When using MVA on a mod-  
 258 elled force-free flux rope, we find that the component tangential to the flux rope is in  
 259 the direction of maximum variance (blue) and the component along the axis of the flux  
 260 rope is in the intermediate direction (yellow). Given the minimum and radial (green) are  
 261 valued at zero.

262 This is not the case at Titan. Adding a slight bend in the flux rope, (shown in fig-  
 263 ure 7) we find that the maximum variance direction (blue) is now nearest aligned to the  
 264 axial direction in a Cartesian sense. Hence, MVA is highly sensitive to small changes in  
 265 the flux rope geometry and as such may lead to problems when fitting models in this man-  
 266 ner. The fitting of orientation angles with associated uncertainty analysis is a physically  
 267 superior method of attempting to fit the force-free model, which results in statistically  
 268 better fittings.

269 An ideal flux rope is usually assumed to have a circular cross-section, and previ-  
 270 ously only a few authors have considered the possibilities of elliptical cross-sections (e.g.,  
 271 Vandas & Romashets, 2017; Nieves-Chinchilla et al., 2018), however none of these are  
 272 for flux ropes in an ionosphere. There are still a number of features in magnetometer data  
 273 that are unable to be replicated with the models shown above, and as such we also in-  
 274 vestigate the ellipticity of the flux rope as a factor that may be causing these deviations  
 275 from perfect circular force-free flux ropes.

276 Evaluating the Bessel functions described in the force-free model in elliptical co-  
 277 ordinates is not trivial and are of the form of Mathieu functions which currently only

278 have a complex valued solution. As such, we assume some simple geometries and avoid  
279 extended use of elliptical co-ordinates in the following solution.

280 At the centre of an ellipse, a central line ( $2c$  in figure 8) is constructed. The ellipse  
281 has a semi-major axis  $a$  and semi-minor axis  $b$  where  $a = b + c$ . A fly-through Cassini  
282 trajectory is then simulated, where each position  $P$  has a unique radial distance  $r$  from  
283 the central line. This radial distance is not valued as the distance from the ellipse centre,  
284 or from the nearest point on the central line. It is found as the distance along a line  
285 extrapolated from the ellipse edge at right-angles to a tangential line, through  $P$  to the  
286 central line (see  $r$  in figure 8).

287 Hence, this value of  $r$  is then used in the elliptical evaluation of the Bessel func-  
288 tions:

$$B_z = B_0 J_0(\alpha r), \quad (19)$$

$$B_v = H B_0 J_1(\alpha r), \quad (20)$$

$$B_u = 0, \quad (21)$$

291 where  $\alpha r$  is evaluated in the same way as the circular force-free model, this model is shown  
292 in elliptical coordinates  $(u, v, z)$ , which are radial, tangential and axial equivalent respec-  
293 tively. The magnetic offset  $b_0$  is not presented in this analysis for simplicity, however can  
294 be easily implemented if need be.

295 Figure 9 shows a flux rope example from T29 at 21:34 on 26/04/2007 at 13.7 SLT  
296 in black along with the fitted model of the elliptical flux rope. This elliptical flux rope  
297 has semi-major axis of 250 km and semi-minor axis of 150 km, and both the undeformed  
298 force-free and non-force-free model were unable to fit to this flux rope with adequate  $\chi^2$   
299 (6.7 and 6.5 nT respectively). Uncertainties are comparable for each fitting method, hence  
300 the lower value of 3.8 nT for the elliptical force-free model fitting can be considered the  
301 best fit from the selected models, and it is likely that this flux rope does not have a cir-  
302 cular cross-section.

303 One example is shown here to emphasise the asymmetrical and plateau properties  
304 of the different components of magnetic field and how these could be caused by an el-  
305 liptical flux rope cross-section. A schematic of the trajectory Cassini could take through  
306 an elliptical flux rope to produce a similar magnetic signature is shown in figure 10. How-  
307 ever, a number of flux ropes show signs of a flat-top in axial field or an asymmetry that  
308 can not be reproduced by bending alone, and as such we show that some ellipticity is  
309 common in flux ropes at Titan.

## 310 4 Discussion

311 In this study, we have examined the differences of fitting a force-free and a non-  
312 force-free model along with exploring different deformations that can be made to the force-  
313 free model which will allow improved fitting and simulation of some magnetic field sig-  
314 natures. A full discussion of the force-free model alone is given in Martin et al. (Accepted),  
315 and as such we will restrict this discussion to the non-force-free model and their com-  
316 parison.

317 The non-force-free model utilises a polynomial expansion of the current density in  
318 the flux rope, and as such allows for much lower  $\chi^2$  results and smaller uncertainties. The  
319 model uses the 3rd order for the axial field and the 4th order for the tangential field, de-  
320 termined to be the optimum balance between improving the fitting and time spent fit-  
321 ting. Increases above the 3rd and 4th orders does not radically improve or change the  
322 fitted parameters.

323 From a total of 85 flux ropes, 84 are fitted with a  $\chi^2$  probability of 5% or less re-  
324 lating to an MSE of 0.5 nT or less, which is the same criteria for a *good* fit for the force-

325 free model. One flux rope is unable to be fitted within the restrictions, which is also a  
 326 flux rope which is unable to be fitted with the force-free assumptions. The remaining  
 327 84 flux ropes give a range of axial magnetic field values of 1-5 nT with a large tail up  
 328 to 40 nT, and flux rope radii of 50- 350 km, again with a large tail up to 1500 km.

329 In comparison, these ranges are smaller than the ranges given from the use of the  
 330 force-free model which has a number of larger values, this however, may be a consequence  
 331 of the far lower number of flux ropes fitted with the force-free model. We show that the  
 332 two models give similar statistical views of the flux rope parameters, however figures 3  
 333 & 4 show examples where both models fit the magnetometer data. With the non-force-  
 334 free model giving much improved  $\chi^2$  values with comparable uncertainties in both ex-  
 335 amples.

336 Table 1 compares the individual parameters retrieved from both models for a pair  
 337 of example flux ropes, where the second example has a much smaller closest approach,  
 338 and values from the two models overlap in uncertainties. The first example shows very  
 339 different parameters for a much larger closest approach. It appears that the difference  
 340 in individual parameters from the two models may be dependent on the closest approach  
 341 value.

342 Figure 11 shows the difference in fitted radii of the flux ropes against the value of  
 343 closest approach. We can see that with small closest approach values the difference be-  
 344 tween the radii given by the models is of a much smaller order. It is apparent that a greater  
 345 closest approach value allows a higher probability of a large disparity between the two  
 346 models and as such we can assume that either model has a strong uncertainty depen-  
 347 dence on closest approach value. Additionally, MVA, though not used in this, has been  
 348 shown to have a similar dependence upon the closest approach values (Xiao et al., 2004).

349 To enable an accurate comparison, both models were fitted using the Bayesian re-  
 350 gression method described earlier. We describe the quality of each fit using the  $\chi^2$  pa-  
 351 rameter, however it is important to calculate and consider the uncertainties on the fit-  
 352 ted values. These uncertainties are derived from the square root of the covariance ma-  
 353 trix diagonal. These values represent the uncertainty of each corresponding parameter  
 354 that is fitted, and most fittings are found to have uncertainty values of 5-10%. Larger  
 355 uncertainties are found, however they are usually comparable to the uncertainties in the  
 356 alternative model and as such we can assume that the  $\chi^2$  parameter is representative of  
 357 the goodness of fit.

358 Current densities and  $\mathbf{j} \times \mathbf{B}$  force density are derived from the magnetic field mod-  
 359 elled or from the model itself for non-force-free.  $\mathbf{j} \times \mathbf{B}$  force density along with field aligned  
 360 currents and current radial to the flux rope are shown for both examples when using the  
 361 non-force-free model. Both examples show zero current density and  $\mathbf{j} \times \mathbf{B}$  force density  
 362 when fitted with a force-free model, which hold for the assumptions of that model. How-  
 363 ever, as the non-force-free model is fitted better, we may then assume that there are quasi-  
 364 field aligned currents along with a  $\mathbf{j} \times \mathbf{B}$  force density in the flux ropes at Titan.

365 This leads to the conclusion that the force-free model is a satisfactory fit for a por-  
 366 tion of flux ropes at Titan, but a much larger number are fitted, and fitted better, by  
 367 the non-force-free model. Therefore, the flux ropes at Titan are more likely to adhere  
 368 to non-force-free assumptions. The implications of which for Titan's magnetosphere as  
 369 a whole can be considerable.

370 Non-force-free structures imply not only the large scale dynamics, such as those  
 371 caused by the surrounding environments and fossil fields, but small scale dynamics as  
 372 well. The results suggest that these are evolving flux ropes which may be a sign that Ti-  
 373 tan's highly variable and dynamic environment is an ideal initiator of flux ropes but does  
 374 not allow them to mature fully before they are disrupted by the upstream conditions at  
 375 Titan. The effects of non-steady-state conditions in Titan's environment are similarly

376 concluded by Cowee et al. (2010), where certain plasma instabilities are unable to evolve  
 377 due to the changes in the upstream conditions at much shorter timescales. Reconnec-  
 378 tion could also be initiated by these small scale re-configurations of the magnetic field  
 379 if the plasma conditions inside the flux rope are not force-free.

380 Additionally, we comment that spatial and temporal changes, such as acceleration  
 381 or deceleration of the flux rope during detection, can also cause asymmetries and changes  
 382 in the magnetic signature of the flux ropes. On the conclusion that a flux rope may not  
 383 be force-free, one may expect some expansion or contraction and this too may change  
 384 the magnetic signatures. These features are outside of the remit of this study, but an  
 385 area for future research.

386 There is no a priori reason why a flux rope has to be perfectly straight and so we  
 387 have developed a model for a bent flux rope. These bent flux ropes allow certain observed  
 388 asymmetries to be modelled reasonably well. We also found that this affected the ori-  
 389 entations of the flux rope as obtained from MVA. A corollary of this is that the appli-  
 390 cation of MVA to observed flux ropes might be systematically affected if the rope is bent.  
 391 A small bend can change the orientation of the tangential and axial field directions which  
 392 may have implications for models of flux ropes in other environments where a flux rope  
 393 may be bent.

394 The assumption that flux ropes are cylindrically symmetric is common, however,  
 395 physically it is unlikely that all flux ropes will be perfectly cylindrical. To that effect,  
 396 the method shown here gives a simple and easy to implement addition to the common  
 397 force-free Bessel function method to fit to and test the elliptical nature of a flux rope.

## 398 5 Summary

399 In this paper we have fitted asymmetrical and non-force free flux rope models to  
 400 Cassini observations of flux ropes in Titan’s ionosphere. These models were fitted us-  
 401 ing Bayesian regression. We have also specifically investigated the role of MVA in mod-  
 402 elling flux ropes and found found higher quality fits when incorporating the orientation  
 403 of the flux rope as explicit fit parameters. However, in the Bayesian framework this does  
 404 not preclude using MVA to inform the priors on the orientation angles.

405 The non-force free model was adapted from Hidalgo et al. (2002) and uses poly-  
 406 nomial expansions for the axial and radial current density in the flux rope. These mod-  
 407 els were found to provide superior fits compared to force-free flux ropes (when account-  
 408 ing for the additional free parameters). This leads to our conclusion that the flux ropes  
 409 at Titan are generally not force-free and in an evolving state.

410 We explored two sources of flux rope asymmetry, bending and ellipticity, and de-  
 411 veloped quantitative modes that were fitted to the data. These bends introduced asym-  
 412 metries in the axial and the radial magnetic field. We specifically found that the pres-  
 413 ence of a small bend in the flux rope would change the result of an MVA analysis of the  
 414 flux rope, and so one would conclude that the orientation was quite different to reality.  
 415 This justifies our approach (following (Nieves-Chinchilla et al., 2016)) of including the  
 416 orientation angles as free parameters in the model. Ellipticity was introduced analyt-  
 417 ically into a force-free flux rope model and was found to produce asymmetries in the ra-  
 418 dial, axial and tangential magnetic fields. A case study was presented where the ellip-  
 419 tical model fitted better than the circular force-free and non-force-free models. These  
 420 flux ropes have a ”plateau” feature in the axial magnetic field that is modelled well by  
 421 the elliptical model, although we note that this may also be caused by a temporal change.

422 These results show that a significant proportion of flux ropes at Titan are non-force-  
 423 free or deformed, suggesting these are evolving flux ropes which may be a sign that Ti-  
 424 tan’s highly variable and dynamic environment is an ideal initiator of flux ropes but does

425 not allow them to mature fully before they are disrupted by the surrounding magneto-  
426 sphere.

427 These conclusions have implications for other planetary bodies, such as Mercury,  
428 where flux ropes are formed and then travel from their source to significant down-tail  
429 distances in seconds (DiBraccio et al., 2015) The models described here can be applied  
430 in many different solar system and plasma contexts.

### 431 Acknowledgments

432 CJM was funded by a Faculty of Science and Technology studentship from Lancaster Uni-  
433 versity. CSA was funded by a Royal Society Research Fellowship. CJM, CSA and SVB  
434 were funded by STFC grant number ST/R000816/1. Cassini MAG data used in this study  
435 may be obtained from the Planetary Data System (<http://pds.nasa.gov/>).

### 436 References

- 437 Ågren, K., Wahlund, J.-E., Garnier, P., Modolo, R., Cui, J., Galand, M., & Müller-  
438 Wodarg, I. (2009). On the ionospheric structure of titan. *Planetary and Space*  
439 *Science*, *57*(14-15), 1821–1827. doi: 10.1016/j.pss.2009.04.012
- 440 Ågren, K., Wahlund, J.-E., Modolo, R., Lummerzheim, D., Galand, M., Müller-  
441 Wodarg, I., ... others (2007). On magnetospheric electron impact ionisation  
442 and dynamics in Titan’s ram-side and polar ionosphere—a Cassini case study.  
443 *Annales Geophysicae*, *25*, 2359–2369. doi: 10.5194/angeo-25-2359-2007
- 444 Burlaga, L. (1988). Magnetic clouds and force-free fields with constant alpha. *Jour-*  
445 *nal of Geophysical Research: Space Physics*, *93*(A7), 7217–7224. doi: 10.1029/  
446 JA093iA07p07217
- 447 Burlaga, L., Klein, L., Sheeley Jr, N., Michels, D., Howard, R., Koomen, M., ...  
448 Rosenbauer, H. (1982). A magnetic cloud and a coronal mass ejection. *Geo-*  
449 *physical Research Letters*, *9*(12), 1317–1320. doi: 10.1029/GL009i012p01317
- 450 Chen, P., & Shibata, K. (2000). An emerging flux trigger mechanism for coronal  
451 mass ejections. *The Astrophysical Journal*, *545*(1), 524. doi: 10.1086/317803
- 452 Cowee, M., Gary, S., Wei, H., Tokar, R., & Russell, C. (2010). An explanation for  
453 the lack of ion cyclotron wave generation by pickup ions at titan: 1-d hybrid  
454 simulation results. *Journal of Geophysical Research: Space Physics*, *115*(A10).  
455 doi: 10.1029/2010JA015769
- 456 Cravens, T., Robertson, I., Clark, J., Wahlund, J.-E., Waite Jr, J., Ledvina, S., ...  
457 others (2005). Titan’s ionosphere: Model comparisons with Cassini Ta data.  
458 *Geophysical Research Letters*, *32*(12). doi: 10.1029/2005GL023249
- 459 DiBraccio, G. A., Slavin, J. A., Imber, S. M., Gershman, D. J., Raines, J. M.,  
460 Jackman, C. M., ... others (2015). Messenger observations of flux ropes  
461 in mercurys magnetotail. *Planetary and Space Science*, *115*, 77–89. doi:  
462 10.1016/j.pss.2014.12.016
- 463 Dougherty, M., Kellock, S., Southwood, D., Balogh, A., Smith, E., Tsurutani, B., ...  
464 others (2004). The Cassini magnetic field investigation. In *The cassini-huygens*  
465 *mission* (pp. 331–383). Springer. doi: 10.1007/s11214-004-1432-2
- 466 Elphic, R., & Russell, C. (1983a). Global characteristics of magnetic flux ropes  
467 in the Venus ionosphere. *Journal of Geophysical Research: Space Physics*,  
468 *88*(A4), 2993–3003. doi: 10.1029/JA088iA04p02993
- 469 Elphic, R., & Russell, C. (1983b). Magnetic flux ropes in the Venus ionosphere:  
470 Observations and models. *Journal of Geophysical Research: Space Physics*,  
471 *88*(A1), 58–72. doi: 10.1029/JA088iA01p00058
- 472 Hidalgo, M., Nieves-Chinchilla, T., & Cid, C. (2002). Elliptical cross-section model  
473 for the magnetic topology of magnetic clouds. *Geophysical research letters*,  
474 *29*(13), 15–1. doi: 10.1029/2001GL013875

- 475 Hughes, W., & Sibeck, D. (1987). On the 3-dimensional structure of plasmoids. *Geo-*  
 476 *physical Research Letters*, *14*(6), 636–639. doi: 10.1029/GL014i006p00636
- 477 Jasinski, J. M., Slavin, J. A., Arridge, C. S., Poh, G., Jia, X., Sergis, N., ...  
 478 Waite Jr, J. H. (2016). Flux transfer event observation at saturn’s dayside  
 479 magnetopause by the cassini spacecraft. *Geophysical Research Letters*, *43*(13),  
 480 6713–6723. doi: 10.1002/2016GL069260
- 481 Keller, C., Cravens, T., & Gan, L. (1992). A model of the ionosphere of Titan.  
 482 *Journal of Geophysical Research: Space Physics*, *97*(A8), 12117–12135. doi: 10  
 483 .1029/92JA00231
- 484 Lepping, R., Berdichevsky, D., & Wu, C.-C. (2017). Average magnetic field mag-  
 485 nitude profiles of wind magnetic clouds as a function of closest approach to  
 486 the clouds axes and comparison to model. *Solar Physics*, *292*(2), 27. doi:  
 487 10.1007/s11207-016-1040-9
- 488 Li, Z., Chen, T., & Yan, G. (2016). New method for determining central axial  
 489 orientation of flux rope embedded within current sheet using multipoint  
 490 measurements. *Science China Earth Sciences*, *59*(10), 2037–2052. doi:  
 491 10.1007/s11430-015-0252-6
- 492 Martin, C., Arridge, C. S., Badman, S. V., Russell, C. T., & Wei, H. Y. (Accepted).  
 493 Distribution and properties of flux ropes in Titan’s ionosphere. *Journal of*  
 494 *Geophysical Research, Space Physics*.
- 495 Mouschovias, T. C., & Poland, A. (1978). Expansion and broadening of coronal loop  
 496 transients—a theoretical explanation. *The Astrophysical Journal*, *220*, 675–682.  
 497 doi: 10.1086/155951
- 498 Ness, N., Acuna, M. H., Behannon, K. W., & Neubauer, F. M. (1982). The induced  
 499 magnetosphere of titan. *Journal of Geophysical Research: Space Physics*,  
 500 *87*(A3), 1369–1381. doi: 10.1029/JA087iA03p01369
- 501 Nieves-Chinchilla, T., Linton, M., Hidalgo, M., & Vourlidas, A. (2018). Elliptic-  
 502 cylindrical analytical flux rope model for magnetic clouds. *The Astrophysical*  
 503 *Journal*, *861*(2), 139. doi: 10.3847/1538-4357/aac951
- 504 Nieves-Chinchilla, T., Linton, M., Hidalgo, M. A., Vourlidas, A., Savani, N. P.,  
 505 Szabo, A., ... Yu, W. (2016). A circular-cylindrical flux-rope analytical  
 506 model for magnetic clouds. *The Astrophysical Journal*, *823*(1), 27. doi:  
 507 10.3847/0004-637X/823/1/27
- 508 Osherovich, V., Farrugia, C., & Burlaga, L. (1995). Nonlinear evolution of mag-  
 509 netic flux ropes: 2. finite beta plasma. *Journal of Geophysical Research: Space*  
 510 *Physics*, *100*(A7), 12307–12318. doi: 10.1029/95JA00273
- 511 Russell, C., & Elphic, R. (1979). Observation of magnetic flux ropes in the venus  
 512 ionosphere. *Nature*, *279*(5714), 616. doi: 10.1038/279616a0
- 513 Russell, C. T., & Elphic, R. (1979). Isee observations of flux transfer events at the  
 514 dayside magnetopause. *Geophysical Research Letters*, *6*(1), 33–36. doi: 10  
 515 .1029/GL006i001p00033
- 516 Slavin, J., Lepping, R. P., Wu, C.-C., Anderson, B. J., Baker, D. N., Benna, M., ...  
 517 others (2010). Messenger observations of large flux transfer events at mercury.  
 518 *Geophysical Research Letters*, *37*(2). doi: 10.1029/2009GL041485
- 519 Sonnerup, B. Ö., & Cahill Jr, L. (1967). Magnetopause structure and attitude from  
 520 explorer 12 observations. *Journal of Geophysical Research*, *72*(1), 171–183. doi:  
 521 10.1029/JZ072i001p00171
- 522 Tsyganenko, N. (1998). Modeling of twisted/warped magnetospheric configurations  
 523 using the general deformation method. *Journal of Geophysical Research: Space*  
 524 *Physics*, *103*(A10), 23551–23563. doi: 10.1029/98JA02292
- 525 Vandas, M., & Romashets, E. (2017). Toroidal flux ropes with elliptical cross sec-  
 526 tions and their magnetic helicity. *Solar Physics*, *292*(9), 129. doi: 10.1007/  
 527 s11207-017-1149-5
- 528 Vignes, D., Acuña, M., Connerney, J., Crider, D., Rème, H., & Mazelle, C. (2004).  
 529 Magnetic flux ropes in the martian atmosphere: Global characteristics. In

- 530 *Mars magnetism and its interaction with the solar wind* (pp. 223–231).  
531 Springer. doi: 10.1023/B:SPAC.0000032716.21619.f2
- 532 Wei, H., Russell, C., Dougherty, M., Ma, Y., Hansen, K., McAndrews, H., . . .  
533 Young, D. (2011). Unusually strong magnetic fields in titans ionosphere: T42 case study. *Advances in Space Research*, 48(2), 314–322. doi:  
534 10.1016/j.asr.2011.02.009
- 535  
536 Wei, H., Russell, C., Zhang, T., & Dougherty, M. (2010). Comparison study of mag-  
537 netic flux ropes in the ionospheres of venus, mars and titan. *Icarus*, 206(1),  
538 174–181. doi: 10.1016/j.icarus.2009.03.014
- 539 Xiao, C., Pu, Z., Ma, Z., Fu, S., Huang, Z., & Zong, Q. (2004). Inferring of flux  
540 rope orientation with the minimum variance analysis technique. *Journal of*  
541 *Geophysical Research: Space Physics*, 109(A11). doi: 10.1029/2004JA010594
- 542 Yelle, R. V., Borggren, N., De La Haye, V., Kasprzak, W., Niemann, H., Müller-  
543 Wodarg, I., & Waite Jr, J. (2006). The vertical structure of titan’s upper  
544 atmosphere from cassini ion neutral mass spectrometer measurements. *Icarus*,  
545 182(2), 567–576. doi: 10.1016/j.icarus.2005.10.029

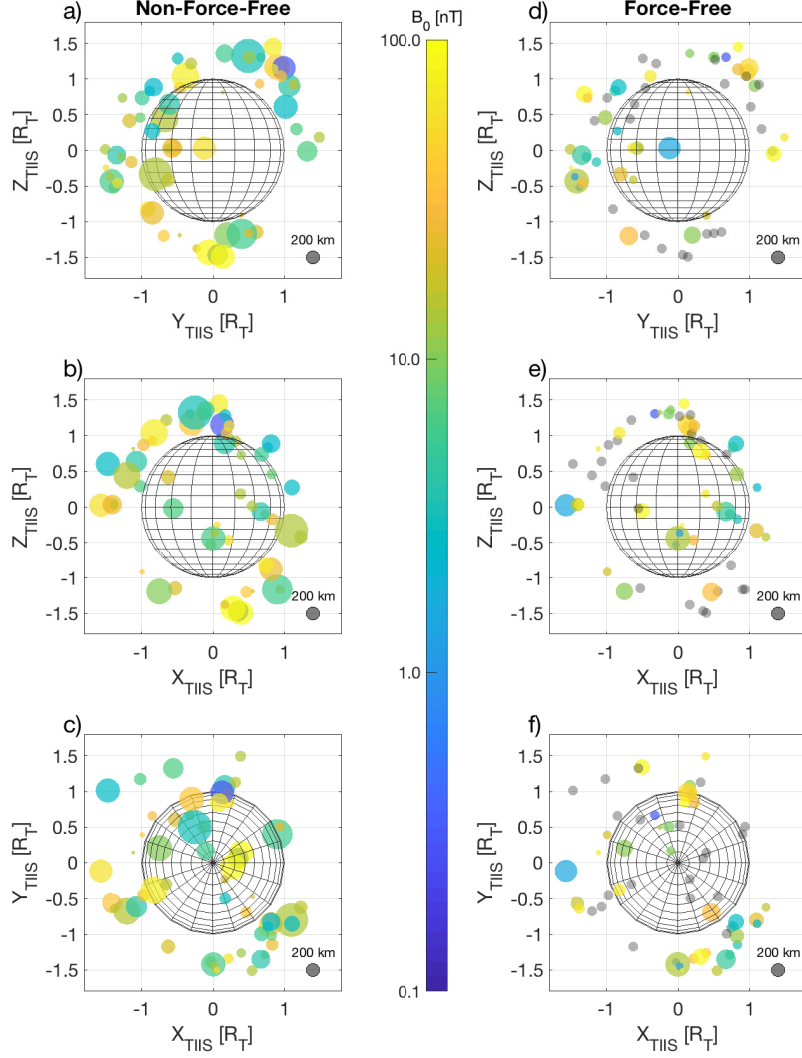


**Figure 1.** Figure showing the position of flux ropes at Titan in the TIIS coordinate system. The size of each point is determined by the radius found using the non-force-free model (a,b,c) and the force-free model (d,e,f), where a 200 km example is shown by the key. Titan's outline is shown in black and each flux rope is a circle coloured by magnetic field strength in the centre of the flux rope. Flux ropes which were not fitted by either model are shown in grey with a 100 km equivalent radius.

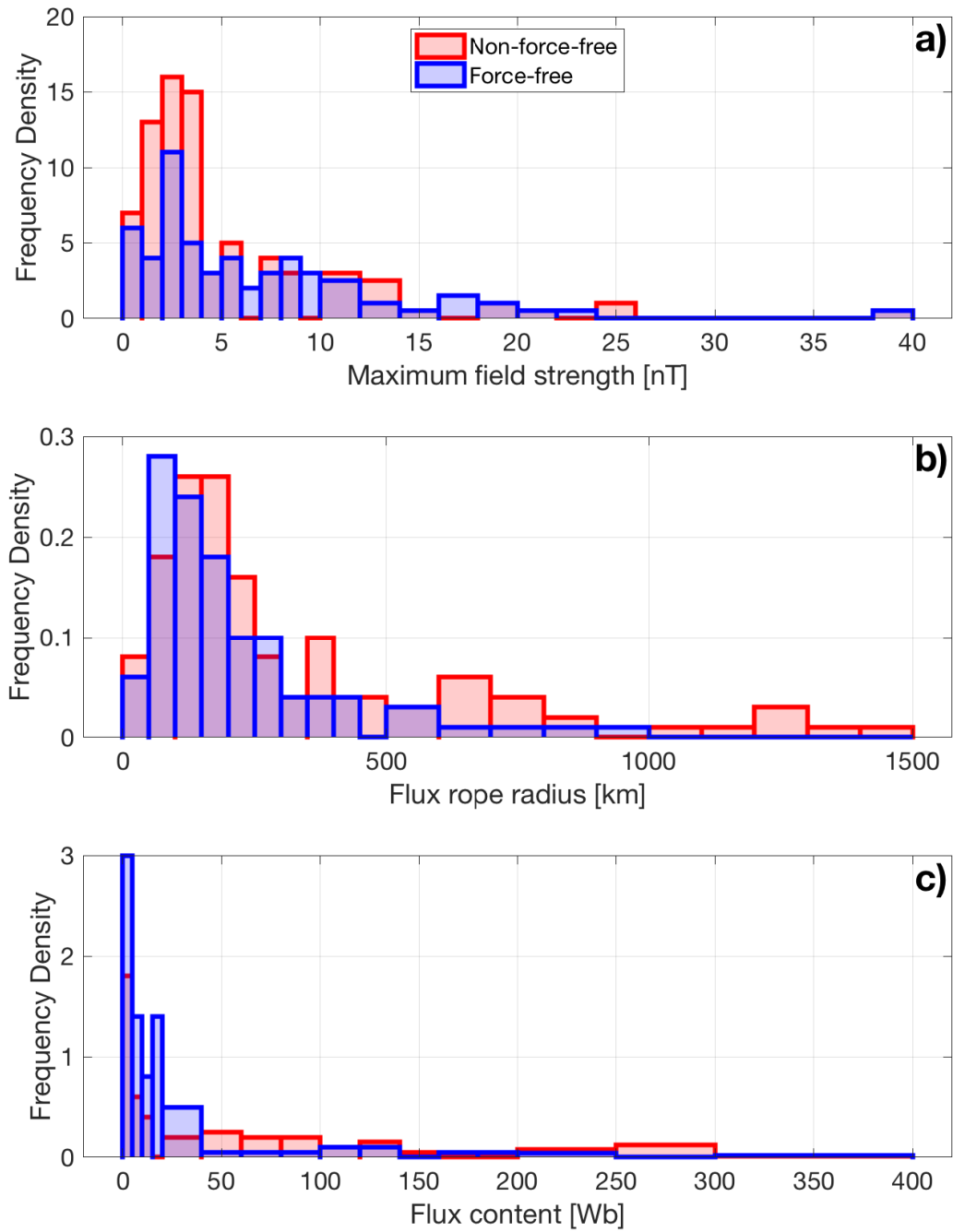


**Figure 2.** Figure comparing a fit of the FF model (blue) and the NFF model (red). a) maximum magnetic field b) flux rope radius and c) flux content

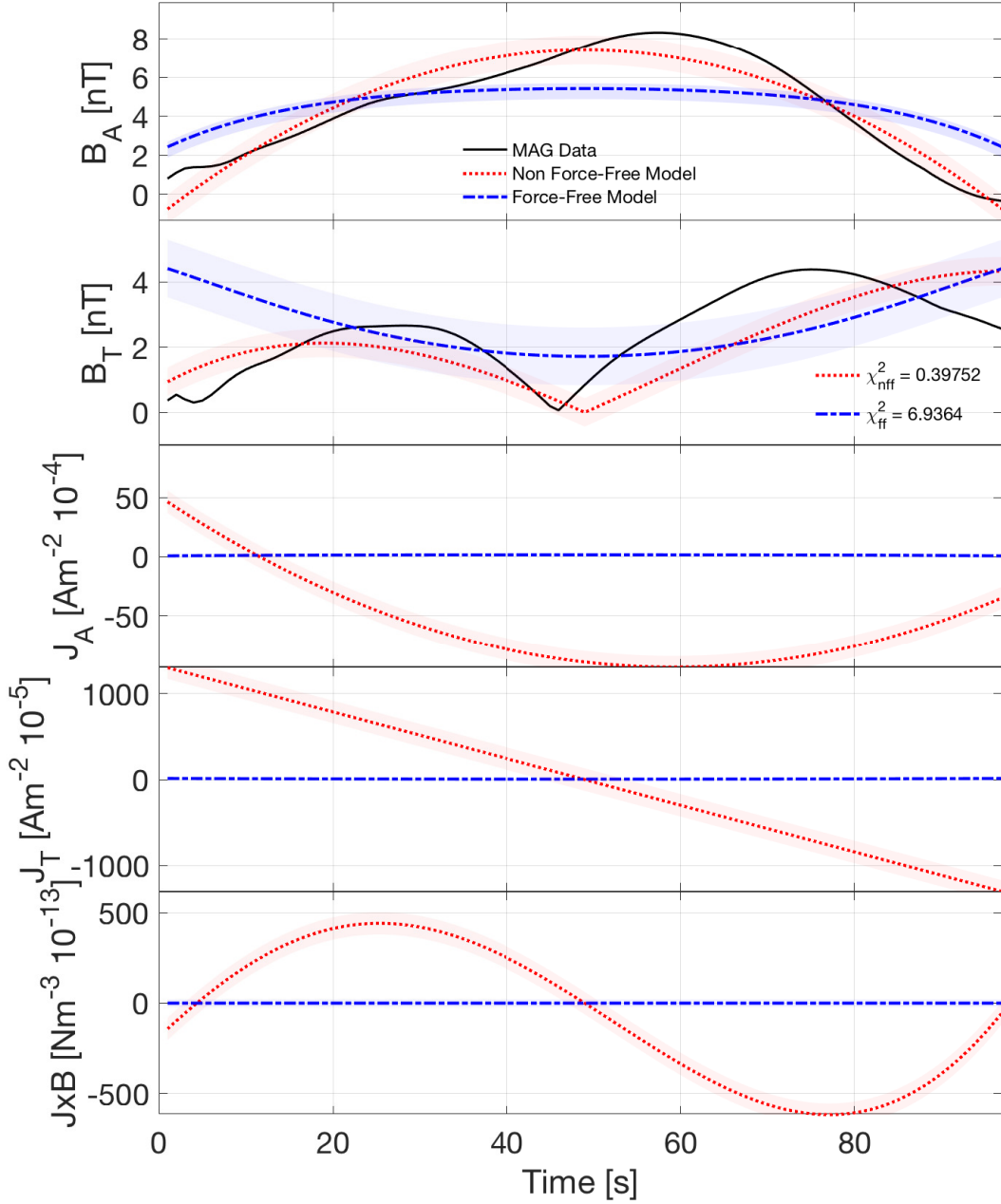


**Figure 3.** Figure comparing a fit of the FF model (blue) and the NFF model (red) with corresponding uncertainty bounds (shaded regions in corresponding colours). The figure shows axial magnetic field, tangential magnetic field, axial current density, tangential current density and force density where data is in black. The corresponding  $\chi^2$  values are shown for each fit. This flux rope is found at 13.6 SLT on T30 at 20:07 on 12/05/2007.

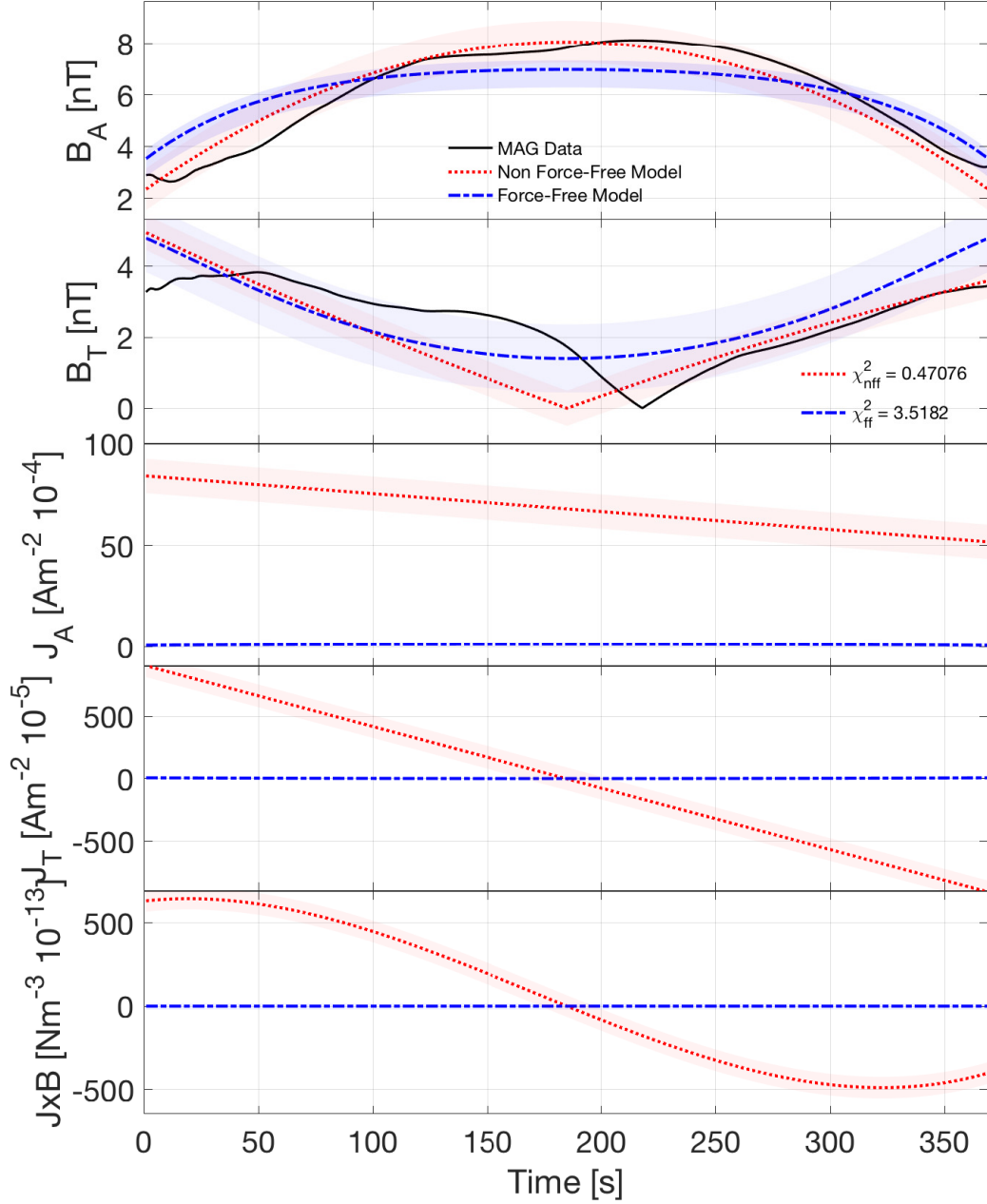


**Figure 4.** Figure comparing a fit of the FF model (blue) and the NFF model (red) with corresponding uncertainty bounds (shaded regions in corresponding colours). The figure shows axial magnetic field, tangential magnetic field, axial current density, tangential current density and force density where data is in black. The corresponding  $\chi^2$  values are shown for each fit. This flux rope is found at 5.3 SLT on T5 at 19:01 on 16/04/2005.

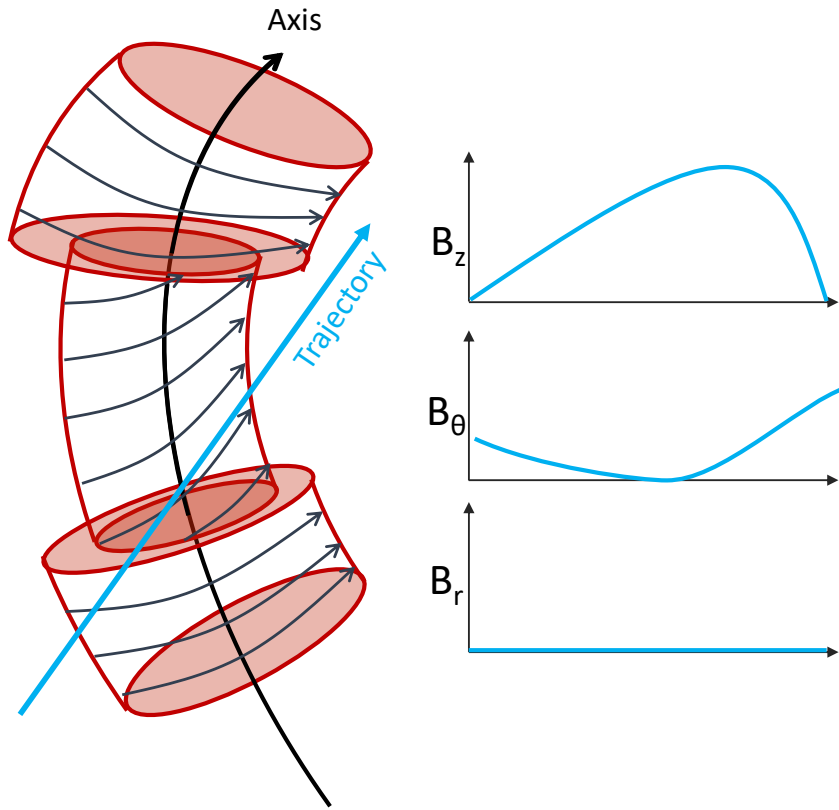


**Figure 5.** Figure showing diagram of a bent flux rope, with simulated fly-through and expected cylindrical magnetic field components.

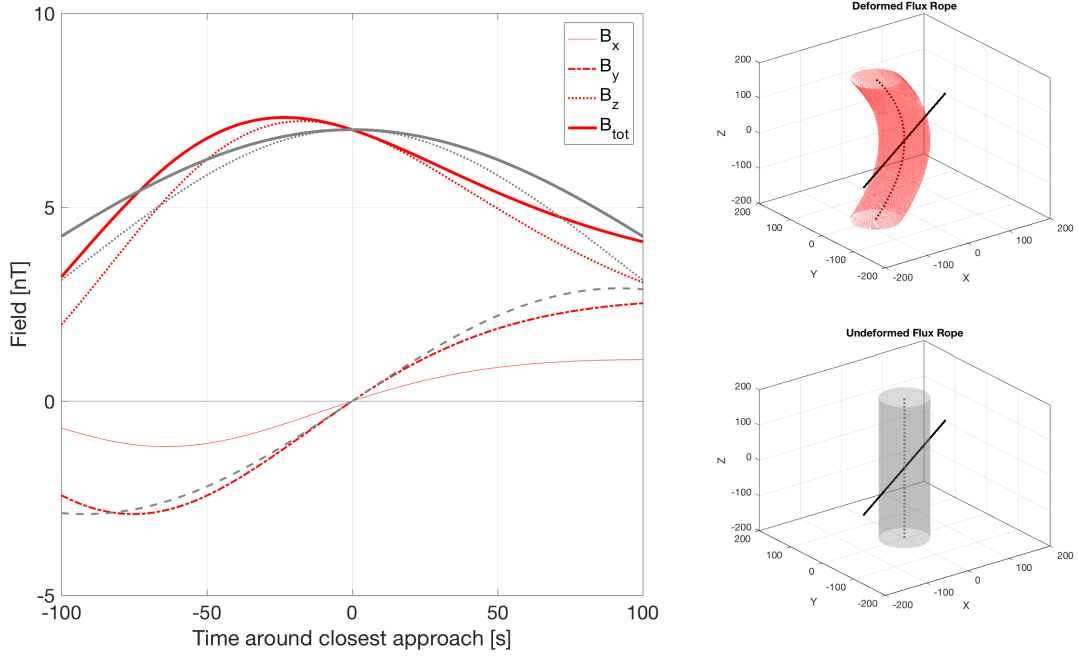


**Figure 6.** Figure showing a comparison of an undeformed flux rope (grey) and a deformed flux rope (red) where the components are total field (thick solid), axial (dotted), y (dash-dot) and x (thin solid).

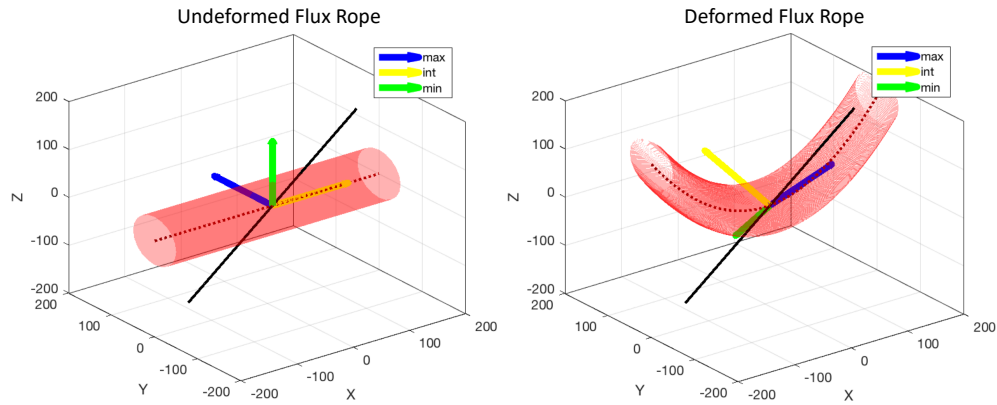


**Figure 7.** Figure showing a comparison of an undeformed flux rope (left) and a deformed flux rope (right) where MVA is used on both and give maximum (blue), intermediate (yellow) and minimum (green) variance directions averaged for the whole fly-through.

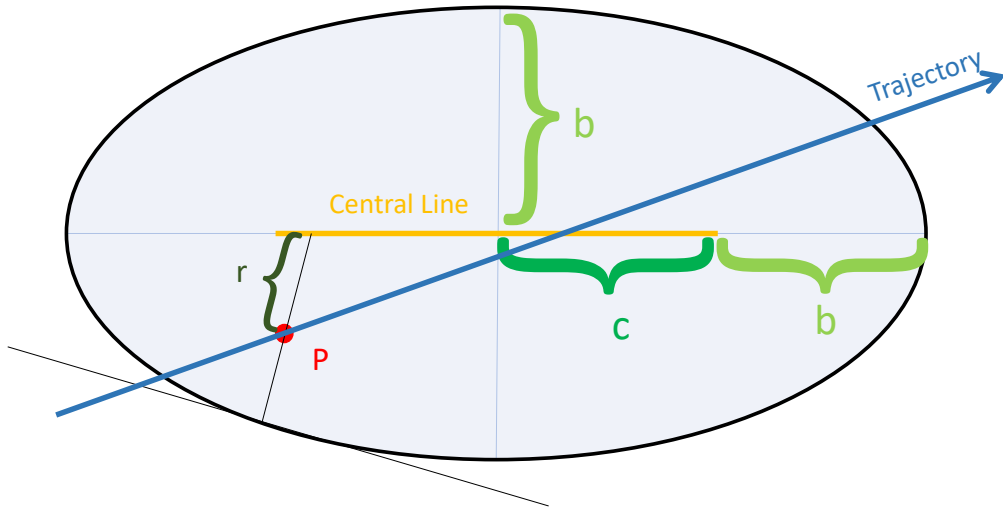


**Figure 8.** Figure showing the cross-section of an elliptical flux rope with model parameters labeled.

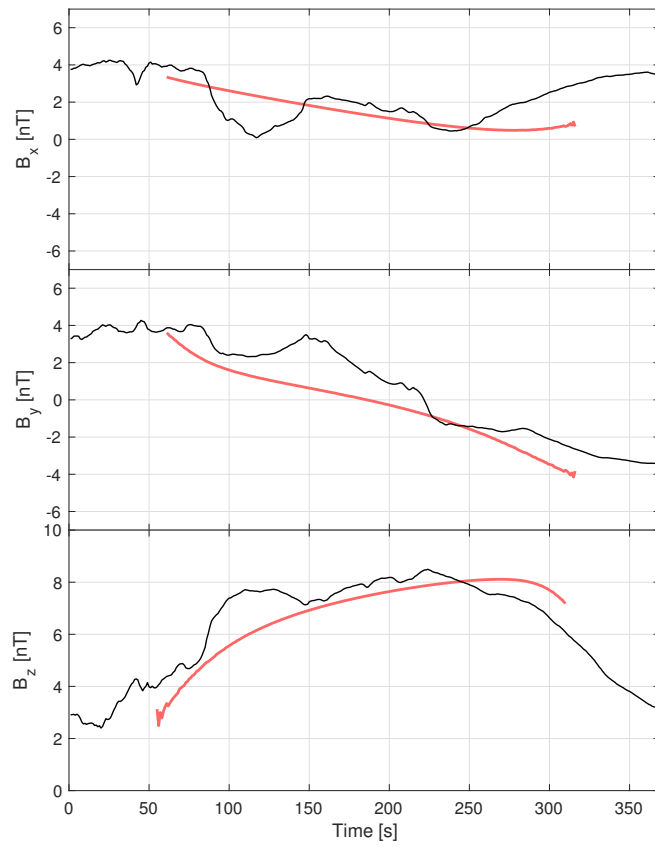


**Figure 9.** Figure showing magnetometer data (black) fitted with the elliptical flux rope model (red) in Cartesian coordinates.

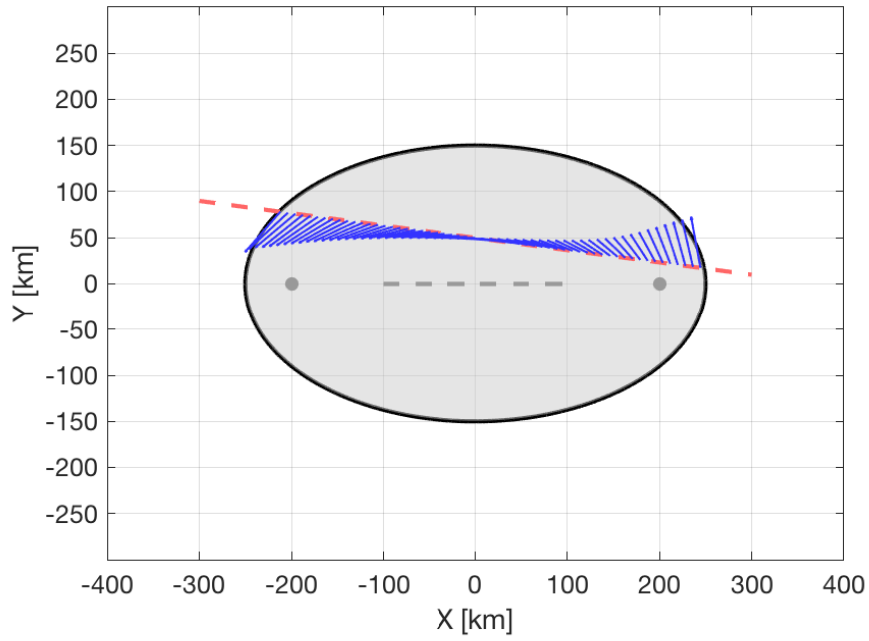


**Figure 10.** Figure showing schematic of set up of trajectory and elliptical flux rope corresponding to fitted magnetometer data in figure 9, where the red dashed line is the expected trajectory, the blue quiver is the model field direction in the x-y plane. The grey shaded area is inside the flux rope and the black solid line is the edge of the flux rope. A dashed grey line shows the central line as described in figure 8 with two grey dots showing the foci of the ellipse.

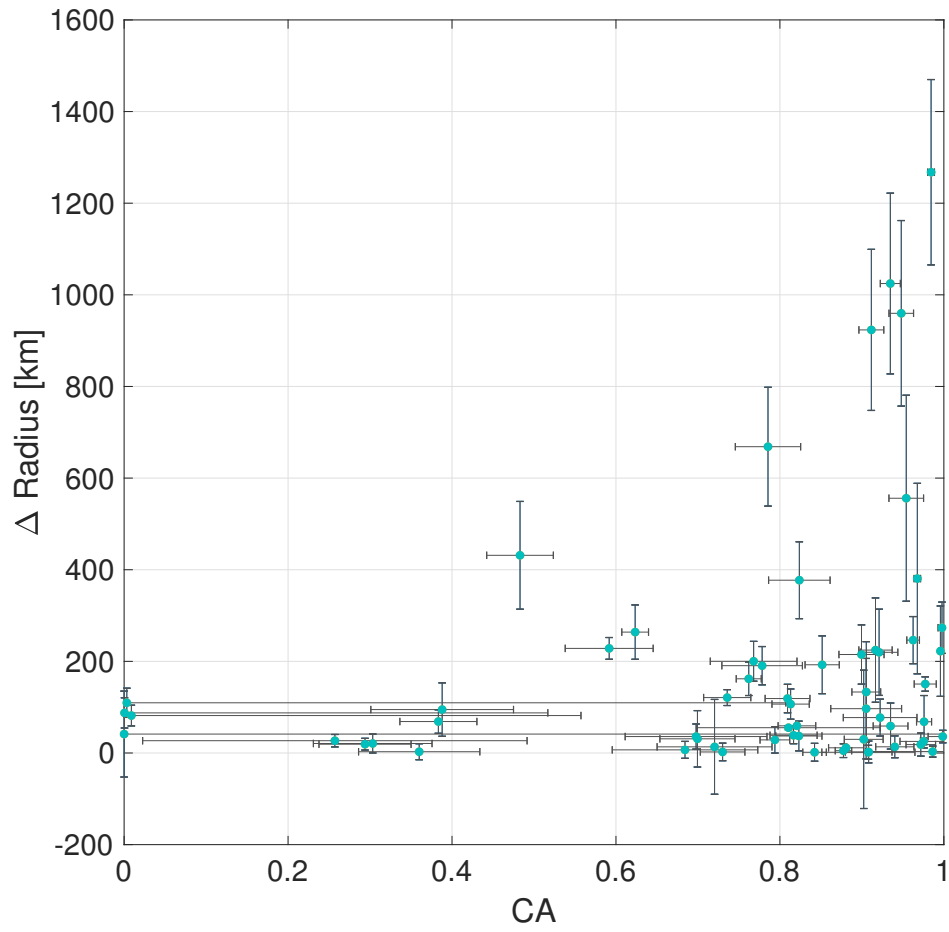


**Figure 11.** Figure showing the increased probability of a disparity between models and CA value.